Enhanced Seamless Transition Control of Grid-Tied Converters Using Dual-eSOGI Vector-Based Synchronization Under Grid Faults

Anupam Nigam, *Graduate Student Member, IEEE*, and Dong-Choon Lee, *Fellow, IEEE*

***Abstract*—This article proposes a vector-based synchronization (VBS) technique using dual-enhanced second-order generalized integrator (eSOGI) for seamless transitions between grid-connected (GC) and standalone (SA) modes. Conventional methods, such as synchronous reference frame phase-locked loops, suffer from slow response and inaccurate voltage estimation during voltage sags, leading to long transients. The proposed VBS using the dual-eSOGI method enables faster and more accurate voltage estimation. An angle alignment method is introduced for presynchronization to enhance performance, minimizing phase mismatches, and frequency transients between the SA and GC transitions. Simulation results on a 1-MW system demonstrate that the proposed method reduces the load fluctuation from 25.75% to 6.89% during unbalanced voltage sag in GC to SA mode transitions and shortens the transition time by 42.26% in SA to GC modes compared to conventional methods. Experimental results on a 1-kW setup validate its effectiveness, demonstrating a stable load current with minimal disturbances.**

***Index Terms*—Grid-connected mode, standalone mode, static transfer switch (STS), synchronization controller, vector-based synchronization.**

TABLE I
TRIP TIMES OF VOLTAGE AND FREQUENCY SPECIFIED IN IEEE 1547 AND IEC 61727

IEEE 1547		IEC 61727	
Voltage range (% of base voltage)	**Trip time (s)**	**Voltage range (% of base voltage)**	**Trip time (s)**
V<50	0.16	V<50	0.10
50<V<88	2.00	50<V<85	2.00
110<V<120	1.00	110<V<135	2.00
V>120	0.16	V>135	0.05
Frequency range (Hz)	**Trip time (s)**	**Frequency range (Hz)**	**Trip time (s)**
f<59.3 or f>60.5	0.16	f<59.3 or f>60.5	0.20

I. INTRODUCTION

VOLTAGE-SOURCE converters (VSCs) have been increasingly used in renewable energy systems, advanced power transmission networks, and electric transportation. Their growing integration is reshaping the dynamics of modern power grids. Unlike conventional synchronous generators, the dynamic behavior of VSCs depends heavily on the control algorithms. Recent reports have highlighted that instability can be introduced by these algorithms under varying grid conditions, leading to issues such as loss of synchronization. These challenges significantly affect the reliability of electricity supply in grids with high levels of renewable energy [1].

In the event of a grid fault, VSCs should be disconnected upon detecting the fault. The fault detection time of converters in response to abnormal grid voltage/frequency conditions are detailed in [2] and outlined by the IEEE 1547 and IEC 61727 standards [3], as specified in Table I. However, during such faults, critical infrastructures within the grid-tied systems are also disconnected from the utility grid, resulting in an interruption of power supply. Therefore, the primary challenge in achieving a seamless transition is to ensure uninterrupted power to critical infrastructures, which should be supplied by VSCs during the transition process. In the standalone (SA) mode, the VSC should switch from current control to voltage control to provide stable voltage to local critical infrastructures [4]. Once the main grid voltage returns to normal, the VSC transitions back to grid-connected (GC) operation. This mode transition typically results in voltage spikes across sensitive loads and rush currents to the main grid. Therefore, achieving a seamless transition between the operation modes is crucial for minimizing these voltage spikes and rush currents.

Despite advancements, several issues and technical challenges remain for the successful integration of renewable energy sources into the utility grid. One of the most critical issues is the synchronization of grid-side converter [5], [6], [7], [8], [9]. This challenge becomes more critical when the utility grid experiences disturbances and unbalanced faults [10]. During such faults, grid-side converters face three major problems: 1) excessive dc-link voltage, 2) high ac current, and 3) loss of grid voltage synchronization.

Received 21 November 2024; revised 6 February 2025 and 11 April 2025; accepted 3 May 2025. Date of publication 12 May 2025; date of current version 30 June 2025. This work was supported by the National Research Foundation of Korea grant funded by the Ministry of Science and ICT of Korea government under Grant RS-2024-00347621. Recommended for publication by Associate Editor J. He. *(Corresponding author: Dong-Choon Lee.)*

The authors are with the Department of Electrical Engineering, Yeungnam University, Gyeongsan 38541, South Korea (e-mail: anupam26@yu.ac.kr; dclee@yu.ac.kr).

Color versions of one or more figures in this article are available at https://doi.org/10.1109/TPEL.2025.3569088.

Digital Object Identifier 10.1109/TPEL.2025.3569088

Most current presynchronization methods rely on a single control loop to align the frequency and phase of two sources using a proportional-integral (PI) based method [11], [12], [13], [14], [15], [16], [17]. These methods typically introduce temporary frequency fluctuations during phase alignment, and the process continues until both parameters align simultaneously. A self-synchronizing synchronverter was proposed in [18], thereby eliminating the need for a dedicated synchronization unit. Synchronverters are inverters that imitate the behavior of synchronous generators, aiding power systems in managing the integration of renewable energy into the grid. They automatically synchronize with the grid before reconnection and follow the grid frequency after transitioning to the GC mode. Despite these benefits, this approach requires an additional mode detection mechanism and exhibits slower response times due to synchronization delays. In addition, it experiences reactive power imbalance issues when used with parallel inverters, limiting its plug-and-play capability.

A virtual torque and flux-linkage-based synchronizing technique was proposed by Ramezani et al. [19]. This technique allows the smooth transition of synchronous inverters from OFF-grid to ON-grid. A presynchronization unit-based method was proposed by Meng et al. [20]. Inverters are enabled to switch between the grid current control and droop control during transitions. These transitions occur between the ON-grid and OFF-grid modes. However, the use of a dedicated inverter-based unit is required for seamless transitions, resulting in a more costly solution. A modified phase-locked loop (PLL) was proposed to achieve seamless transitions for three-phase GC inverters in [21]. The phase of the load voltage is synchronized with the grid voltage in the reconnection mode using a dq-based PLL, whereas in the SA mode, a phase of the desired frequency is generated. However, the system response is significantly degraded under unbalanced and distorted grid voltage conditions. Several presynchronization methods, including the proposed method, are summarized in Table II.

TABLE II
SUMMARY OF EXISTING PRESYNCHRONIZATION METHODS

Ref.	Pros and Cons
PI-based method [11]-[17]	• Voltage and phase differences between the converter and grid sides are regulated to zero. • Phase error between the grid and converter converter sides is calculated, based on which transitions between modes are made until stabilization at the final state. • Challenges in tuning and rapid mode transitions arise due to the slow response in synchronization.
Self-synchronizing synchronverter [18]	• Dedicated PLL for synchronization is not required. • Response time is slow due to the need to synchronize time. • New configuration is required during the transition between the GC and SA modes.
VT and VFL - based synchronization [19]	• Simple and effective approach for synchronizing phase and voltage amplitude in synchronverters ensures reliable performance. • Tuning of controller is highly sensitive to gains. • Due to inherent property of synchronverter, the response is slower.
PLL-based sequence [21]	• Grid and converter voltage phases are synchronized by the PLL. • Under grid fault conditions, the system response degrades significantly. • There are challenges in implementing PLLs.
Angle alignment method (Proposed)	✓ Implementation is easy and simple. ✓ No tuning is required. ✓ System response is fast.

Various three-phase grid synchronization under distorted and unbalanced conditions have been proposed in the technical literature. The synchronous reference frame-PLL (SRF-PLL) remains one of the most popular synchronization techniques [22], [23]. Despite the good performance of the SRF-PLL under balanced grid conditions, its effectiveness degrades when the three-phase input signal becomes unbalanced or distorted. PLL-based synchronization techniques use a PI controller to obtain the angular frequency, which must be tuned for a specific system [24], [25]. In the PLL, both the frequency and phase angle are calculated in the same loop. Changes in the phase angle result in transients in the frequency, which are reflected onto the phase angle, leading to delays during synchronization process. In addition, when the PLL begins to operate, there is a significant initial phase angle difference between the input voltage signal and the PLL integrator, and a delay in presynchronization is observed.

This article extends the work presented in [26], which introduces a seamless transition strategies for grid-tied systems using SRF-PLL for grid phase estimation. Unlike other methods, the proposed control approach employs a vector-based synchronization (VBS) scheme using a dual-enhanced second-order generalized integrator (eSOGI) for grid voltage phase estimation, enabling the synchronization of the modular multilevel converter (MMC) to the grid. This method represents the three-phase grid voltage as two vectors on the α–β plane. The major benefit of this technique is that no PLL is used. As a result, the VBS technique using the eSOGI method offers a simpler and faster solution compared to PLL-based techniques, particularly in terms of system-level operation and practical implementation for synchronization under dynamic grid conditions. Moreover, as an open-loop technique for grid voltage estimation, it operates without feedback, allowing instantaneous changes in the grid to be directly observed. For the presynchronization method, angle alignment method is used for the transition from VBS technique to power synchronization control (PSC). This angle alignment method depends upon the final value of the previous mode for the initial value of next mode. This scheme is better than the PI-based method, which requires tuning and has a slow response. The main contributions of this article are as follows.

1) A detailed overview of the problems associated with the conventional SRF-PLL with the PI-based presynchronization method during grid faults.

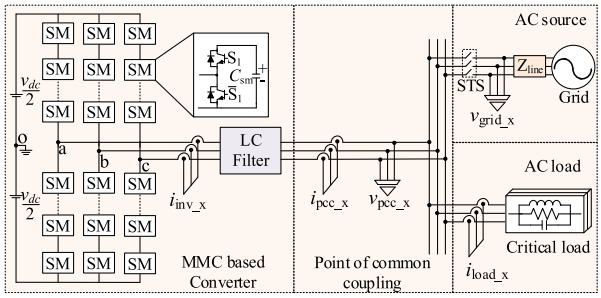

Fig. 1. Circuit configuration of the grid-tied system.

2) Accurate voltage estimation during the voltage sag or swell in the GC mode by VBS using the dual-eSOGI synchronization method.
3) Proposed angle alignment presynchronization technique for transitioning between the GC and SA modes for a continuous supply of the load even in the absence of a grid.
4) A comparison between the conventional and proposed methods during mode transitions, demonstrated through both simulation and experimental results.

II. Overview of the Conventional SRF-PLL Control Scheme

A. System Description

Fig. 1 illustrates the circuit configuration of a grid-tied system, comprising a three-phase converter (MMC), an *LC* filter, a critical load, and the grid, where x represents the a, b, and c phases, $v_{\rm dc}$ denotes the dc-link voltage; $v_{\rm pcc\_x}$ denotes the voltages at the PCC; $v_{\rm grid\_x}$ denotes the grid voltages; $i_{\rm inv\_x}$ denotes the converter output currents; $i_{\rm pcc\_x}$ denotes the PCC currents after an *LC* filter, and $i_{\rm load\_x}$ denotes the load currents. The converter controls a static transfer switch (STS) between the critical load and the ac grid. This approach can be used to disconnect the critical load from the ac grid when a grid fault is detected, causing the system to transition to the SA mode.

The conventional control strategy, as illustrated in Fig. 2 integrates an SRF-PLL and a PSC to establish the frequency and phase angle for the GC and SA modes, respectively. The control strategy maintains a consistent current control approach across both modes. However, the reference points for the current loop vary depending on the operational mode. In the SA mode, the system relies on a voltage control loop, whereas in the GC mode, it adheres to a power control loop.

The $\theta_{\rm g}$ and $\theta_{\rm r}$ represent the phase angle generated by the SRF-PLL for the GC mode and by the PSC for the SA mode, respectively. $v_{\rm pcc\_d}$ and $v_{\rm pcc\_q}$ are obtained from the *dq*-transformation of three phase PCC voltages. Similarly, $i_{\rm pcc\_d}$ and $i_{\rm pcc\_q}$ are dq-axis PCC currents. $i^*_{\rm gfl\_d}$ and $i^*_{\rm gfl\_q}$ are the references, which are input of the current controller for GC mode. $P_{\rm ref}$ and $Q_{\rm ref}$ are the active and reactive power references. $i^*_{\rm gfm\_d}$ and $i^*_{\rm gfm\_q}$ are the *dq*-axis current references for SA mode. During the transition, the output of S_1 is added to either position "1" or "2", depending on the previous mode in the synchronization controller. This adjustment helps obtain synchronized θ, which is used for the *dq*-transformation.

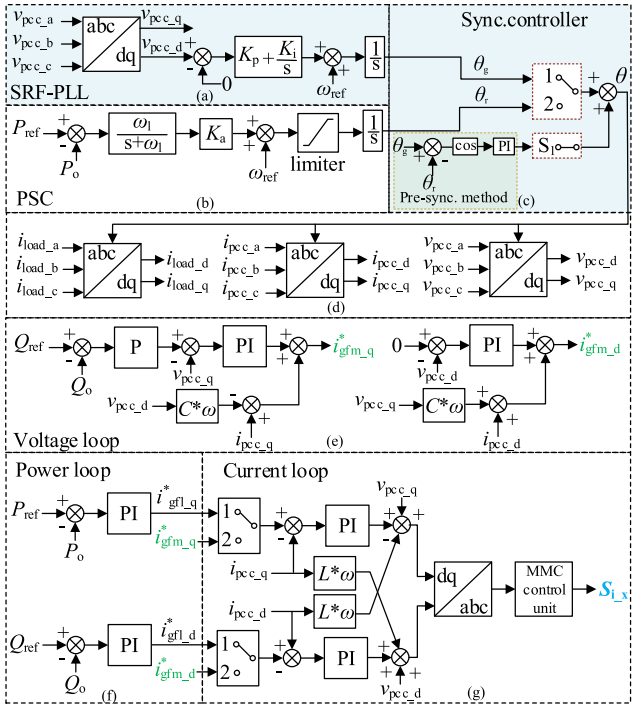

Fig. 2. Conventional control strategy for seamless transition between GC and SA modes. (a) SRF-PLL for GC mode. (b) PSC for SA mode. (c) Synchronization controller. (d) Signal *dq*-transformation. (e) Voltage loop for SA mode. (f) Power loop for GC mode. (g) Current loop for the two modes.

B. Mathematical Analysis of SRF-PLL

As shown in Fig. 2, the dynamic equation governing the SRF-PLL can be expressed as follows:

$$\theta_{\rm g} = \int \left[\omega_{\rm g} + (K_{\rm p} + K_{\rm i}\int)(v_{\rm pcc\_q} - 0)\right] \tag{1}$$

where $\omega_{\rm g}$ represents the nominal grid frequency, and $K_{\rm p}$ and $K_{\rm i}$ are the proportional and integral gains of the PI controller, respectively. $v_{\rm pcc\_q}$ denotes the q-axis component of the PCC voltage, which can be calculated as follows:

$$v_{\rm pcc\_q} = v_{\rm z\_q} + v_{\rm grid\_q} \tag{2}$$

where $v_{\rm z\_q}$ and $v_{\rm grid\_q}$ represent the q-axis voltage component across the line impedance and the q-axis grid voltage, respectively. The line impedance is given by $Z_{\rm line} = R_{\rm line} + {\rm j}X_{\rm line}$, and the expressions for $v_{\rm z\_q}$ and $v_{\rm grid\_q}$ can be derived as follows:

$$v_{\rm z\_q} = i_{\rm pcc\_d} \cdot X_{\rm line} + i_{\rm pcc\_q} \cdot R_{\rm line} \tag{3}$$

$$v_{\rm grid\_q} = v_{\rm grid} \cdot \sin(\theta_{\rm e} - \theta_{\rm g}) \tag{4}$$

where $\theta_{\rm e}$ represents the ideal source voltage angle.

The phase angle difference between $\theta_{\rm g}$ and $\theta_{\rm e}$ as δ

$$\delta = \theta_{\rm g} - \theta_{\rm e}. \tag{5}$$

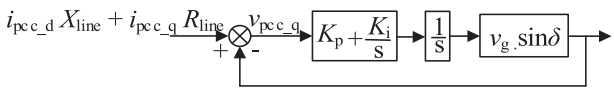

Fig. 3. Equivalent diagram of SRF-PLL considering the effect of line impedance.

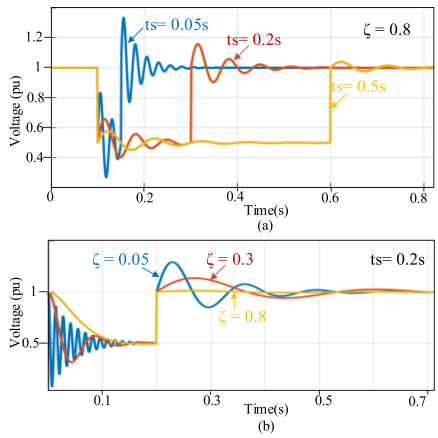

Fig. 4. Parametric effects of PLL during voltage sag and recovery between 0.5 and 1 p.u. (a) Fixed damping factor (ζ) with varying settling times (t_s). (b) Fixed settling time (t_s) with varying damping factors (ζ).

Substituting (2) through (5) into (1), and considering the integral relationship $\theta_e = \int \omega_g dt$, δ is obtained as

$$\delta = \int (K_p + K_i \int)(i_{pcc\_d}.X_{line} + i_{pcc\_q}.R_{line} - v_{grid}.\sin\delta). \tag{6}$$

Thus, the second-order phase swing behavior of the PLL, considering the converter-grid interaction, is described in (6). Therefore, an equivalent diagram of the SRF-PLL is illustrated in Fig. 3.

C. Parametric Effect of PLL on GC Converters

As a second-order dynamic system, the PLL is typically characterized by two key parameters: 1) the damping ratio (ξ) and 2) the settling time (t_s). These parameters can be expressed in terms of the PLL controller parameters as follows [27]:

$$\xi = \frac{K_p}{2}\sqrt{\frac{v_{gn}}{K_i}} \tag{7}$$

$$t_s = \frac{9.2}{v_{gn}K_p} \tag{8}$$

where v_{gn} is the nominal grid voltage.

1) *Effects of the Settling Time of the PLL*:

Fig. 4(a) shows the influence of different settling times on system performance, with the damping ratio fixed at 0.8. The voltage sag ranges from 1 p.u. to 0.5 p.u. Among the various settling times considered, a t_s of 0.05 s produces the most significant oscillation during the transition from 1 to 0.5 p.u. In contrast, a t_s of 0.5 s results in much more stable behavior throughout the transition. In addition, during the recovery to 1 p.u. using the presynchronization method, the most prominent oscillation occured with the faster t_s of 0.05 s, whereas a t_s of 0.5 s provided a smoother recovery.

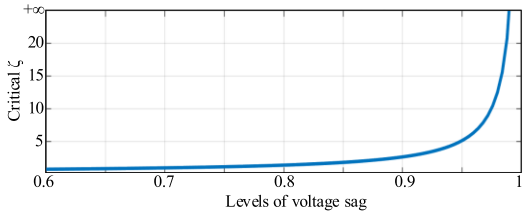

Fig. 5. Critical damping ratio (ζ) under varying levels of voltage sag.

2) *Effects of the Damping Ratio of the PLL*:

Fig. 4(b) shows the impact of varying damping ratios on system performance, with the settling time fixed at 0.2 s. The voltage sag ranges from 1 p.u. to 0.5 p.u. Among the different damping ratios, a ξ of 0.05 generates the highest level of oscillation during the voltage sag and recovery to 1 p.u. when using the pre-synchronization method. A ξ of 0.3 results in reduced oscillation compared to 0.05, whereas a ξ of 0.8 provides the most stable performance with minimal oscillatory behavior.

It is important to highlight that, although a damping ratio of 0.707 is typically selected for tuning the PLL parameters, this value may not be appropriate when addressing the voltage sag in a converter. As demonstrated in (3)–(6), the dynamics of δ are influenced not only by the postfault grid voltage but also by the q-axis voltage drop across the line impedance. Fig. 5 shows the critical damping ratios for different voltage sag levels. As the voltage sag level increases, a higher critical damping ratio is required.

Thus, two important conclusions can be drawn from the above discussions.

1) As Ki increases, the damping ratio decreases, leading to increased oscillations in the system.
2) As the voltage sag increases, a higher critical damping ratio is required to minimize the oscillations and stabilize the system.

D. Effect of PI- Based Presynchronization Method

This approach typically uses a PI controller to process either the phase error or the sine of the phase error, thereby introducing temporary frequency adjustments to facilitate phase alignment. However, when this control loop is activated, it often results in a frequency fluctuation, the extent of which depends on the phase error. Although the phase may align, the frequency can drift, leading to a subsequent misalignment of the phase. This interaction persists as the control loop continues to operate and terminates, only when both parameters achieve their target values simultaneously. In addition, the frequency of the incoming source is usually assumed to remain constant during synchronization; however, in the case of a weak source, its frequency variations due to disturbances can lead to further mismatches in frequency and/or phase, prolonging the process. With this method, θ is obtained as follows:

$$\theta(t) = \theta(t-1) + K_p\{\cos(|err|(t)) - \cos(|err|(t-1))\} + K_i\cos(|err|(t)) \tag{9}$$

where $err = \theta_g - \theta_r$.

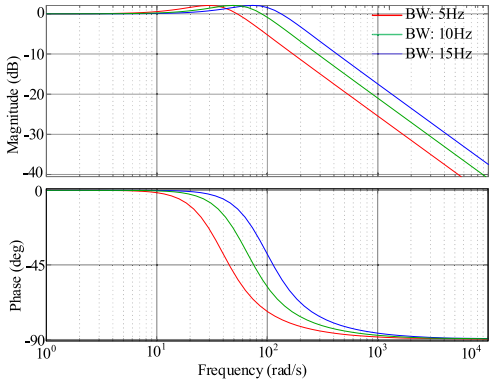

Fig. 6. Bode plot of PI-based method.

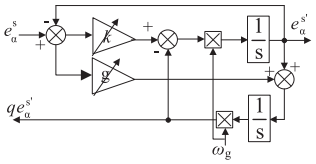

Fig. 7. Enhanced SOGI structure.

The design of the controller gain follows the approach in [24], with the optimal value selected and validated through the Bode plot in Fig. 6. For a critically damped response ($\zeta \approx 0.707$), the Bode plots for the PI-based method illustrate the tradeoffs between bandwidth and phase margin. A higher bandwidth (15 Hz) maintains the phase response closer to 0° over a wider frequency range, enhancing responsiveness but increasing the risk of instability in weak grids. Conversely, a lower bandwidth (5 Hz) ensures stability and robustness in weak-grid scenarios but slows phase tracking. The selected 10 Hz bandwidth effectively filters harmonics and noise while maintaining sufficient responsiveness for synchronization during voltage sags and swells. Its optimal selection is guided by stability margins and dynamic performance, ensuring adequate phase margin without excessive response delay.

III. Proposed Scheme For Seamless Transition

A. VBS Using the Dual-eSOGI Method for GC Mode

In the GC mode, the converter operates in power control mode, whereas in the SA mode it transitions to voltage control mode. The key to this seamless transition is the timely and accurate detection of grid voltage sag, which necessitates a reliable system [28]. During grid fault conditions, errors in estimating grid voltages, which are used to determine the grid angle and generate grid current references, can worsen fluctuations in grid-side power. The improved DSOGI-PLL ensures robust synchronization under stable conditions, it faces challenges in adapting to sudden grid frequency variations, which can impact its effectiveness in grid dynamic operations [29]. To address these issues, the VBS technique using the dual-eSOGI method is proposed to obtain accurate grid voltage estimation.

In contrast to the standard SOGI, a variable gain g is added to the eSOGI, as depicted in Fig. 7. This gain provides additional

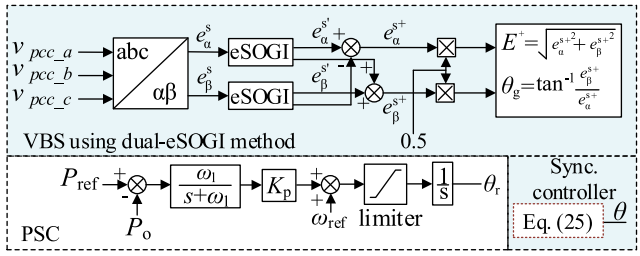

Fig. 8. Proposed synchronization technique using eSOGI method.

flexibility to improve the dual-eSOGI transient performance. The values of k and g were adjusted according to the estimated amplitude of the grid voltage positive-sequence component (E^+) and a threshold (σ) [28] as follows:

$$k = \begin{cases} k_{\text{steady}} & (dE^+/dt) < \sigma \\ k_{\text{sag}} & (dE^+/dt) \geq \sigma \end{cases} \tag{10}$$

$$g = \begin{cases} 0 & (dE^+/dt) < \sigma \\ g_{sag} & (dE^+/dt) \geq \sigma \end{cases} \tag{11}$$

where k_{steady}, k_{sag}, and g_{sag} are constant. The superscript "+" denotes the positive-sequence component. The abnormal grid voltage conditions can disrupt the accurate calculation of the grid voltage vector. Therefore, it is essential to extract the accurate positive sequence components of the voltage. The in-phase and quadrature components of e_α^s are calculated using eSOGI, as shown in Fig. 7.

B. Determination of eSOGI Parameters

The proposed synchronization technique is depicted in Fig. 8. The in-phase component ($e_\alpha^{s'}$) of e_β^s is derived as follows:

$$\frac{e_\alpha^{s'}(s)}{e_\alpha^s(s)} = \frac{k\omega_{\text{g}} s - g\omega_{\text{g}}^2}{s^2 + k\omega_{\text{g}} s + (1-g)\omega_{\text{g}}^2}. \tag{12}$$

The in-phase component represents the band-pass filtered output of the input signal, which is characterized by unity gain and a 0° phase shift. In addition, the quadrature component ($qe_\alpha^{s'}$) of qe_α^s is derived as follows:

$$\frac{qe_\alpha^{s'}(s)}{e_\alpha^s(s)} = \frac{k\omega_{\text{g}}^2 + g\omega_{\text{g}} s}{s^2 + k\omega_{\text{g}} s + (1-g)\omega_{\text{g}}^2}. \tag{13}$$

Consequently, the quadrature component is the low-pass filtered output of the input signal, exhibiting unity gain and a 90° phase shift. Similarly, the in-phase and quadrature components of e_β^s are determined as $e_\beta^{s'}$ and $qe_\beta^{s'}$ using the eSOGI method.

Assuming that $e_\alpha^s = A\cos(\omega_g t) + \sum_{x=2}^{\infty} A_x \cos(\omega_x t)$ and $e_\beta^s = A\sin(\omega_g t) + \sum_{x=2}^{\infty} A_x \sin(\omega_x t)$ where x represents the harmonic order and $\omega_x = x\omega_g$, the outputs $e_\alpha^{s'}$, $qe_\alpha^{s'}$, $e_\beta^{s'}$, and $qe_\beta^{s'}$ are derived under steady-state operation from (12) and (13) as

$$e_\alpha^{s'} = A\cos(\omega_g t) + \sum_{x=2}^{\infty} H_x \cos(\omega_x t + a\tan(\Phi_x)) \tag{14}$$

$$qe_{\alpha}^{s'} = A\sin(\omega_g t) + \sum_{x=2}^{\infty} H_{qx}\sin(\omega_x t + a\tan(\Phi_{qx})) \quad (15)$$

$$e_{\beta}^{s'} = A\sin(\omega_g t) + \sum_{x=2}^{\infty} H_{x}\sin(\omega_x t + a\tan(\Phi_{x})) \quad (16)$$

$$qe_{\beta}^{s'} = -A\cos(\omega_g t) - \sum_{x=2}^{\infty} H_{qx}\cos(\omega_x t + a\tan(\Phi_{qx})) \quad (17)$$

where

$$H_x = A_x\omega_g\sqrt{\frac{(k\omega_x)^2 + (g\omega_g)^2}{(k\omega_x\omega_g)^2 + (\omega_g^2 - \omega_h^2 - g\omega_g^2)^2}}$$

$$\Phi_x = \frac{k\omega_x(\omega_g^2 - \omega_x^2)}{k^2\omega_x^2\omega_g - g\omega_g(\omega_g^2 - \omega_x^2 - g\omega_g^2)}$$

$$H_{qx} = A_x\omega_g\sqrt{\frac{(k\omega_g)^2 + (g\omega_x)^2}{(k\omega_x\omega_g)^2 + (\omega_g^2 - \omega_h^2 - g\omega_g^2)^2}}$$

$$\Phi_{qx} = \frac{k\omega_x(\omega_g^2 - \omega_x^2 - g\omega_g^2 + g\omega_x^2)}{k^2\omega_x\omega_g^2 + g\omega_x(\omega_x^2 - \omega_g^2 + g\omega_g^2)}.$$

From (14)–(17), significant harmonics can arise in the estimated positive- and negative-sequence components under distorted grid conditions when a large g value is used. To minimize the impact of these grid voltage harmonics, g should be set to zero under such conditions by properly selecting σ as in (11).

The positive sequence components of the grid voltage $e_{\alpha\beta}^{s+}$ is obtained as

$$e_{\alpha}^{s+} = 0.5(e_{\alpha}^{s'} - qe_{\beta}^{s'}) \quad (18)$$

$$e_{\beta}^{s+} = 0.5(qe_{\alpha}^{s'} + e_{\beta}^{s'}). \quad (19)$$

The magnitude and phase angle of grid voltage are given, respectively, by

$$E^{+} = \sqrt{e_{\alpha}^{s+2} + e_{\beta}^{s+2}} \quad (20)$$

$$\theta_g = \tan^{-1}\frac{e_{\beta}^{s+}}{e_{\alpha}^{s+}}. \quad (21)$$

Assuming k and g are set to k_{sag} and g_{sag}, respectively, under the grid voltage sag or swell conditions, the poles of transfer function is derived as

$$s_{1,2} = -k\omega_g/2 \pm \omega_g\sqrt{k_{sag}^2 - 4(1 - g_{sag})}/2. \quad (22)$$

If g_{sag} is chosen as

$$g_{sag} = -\alpha.k_{sag}^2/4 \quad (23)$$

where α is a constant ranging from $0 < \alpha \leq 1$. The poles $s_{1,2}$ in (22) are rewritten as

$$s_{1,2} = -k_{\text{sag}}\omega_g/2 \pm j\omega_g\sqrt{k_{sag}^2(1 - \alpha) - 1}/2. \quad (24)$$

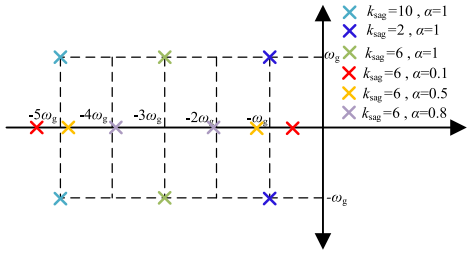

Fig. 9. Root Locus of eSOGI.

The parameter α plays a key role in determining the damping behavior of the system. When α equals 1, the system exhibits an underdamped response, which results in a faster response time but introduces oscillations. Increasing the value of k_{sag} in this case can lead to a more pronounced oscillatory behavior. For α values less than 1, the system becomes overdamped, removing oscillations but slowing the response. Therefore, the choice of k_{sag} and α compromises response time and stability, allowing for flexibility based on the system performance requirements.

C. Analysis of Root-Locus Using Different Values of K_{sag} and g_{sag}

Fig. 9 shows the root locus for different values of k_{sag} and α, illustrating how the system poles shift in the complex plane as these parameters vary. The positions of the poles are critical in determining the system stability and response characteristics. For $k_{sag} = 2$ and $\alpha = 1$, the poles are located close to the imaginary axis, suggesting a moderately fast response with minimal oscillations due to underdamping. Similarly, for $k_{sag} = 10$ and $\alpha = 1$, the poles exhibited a faster response, but with some oscillations due to underdamped behavior. In contrast, for $k_{sag} = 6$ with $\alpha = 0.8$, the system is overdamped, implying that the poles are located further into the real axis, resulting in a slower response but with no oscillations. This behavior changes for $k_{sag} = 6$ and $\alpha = 1$, where the system is underdamped, providing the fastest response but at the cost of oscillatory behavior. Ultimately, selection of $k_{sag} = 6$ and $\alpha = 1$ is preferred in this analysis to achieve the fastest response during the transition from the GC to SA mode operations. This configuration strikes a balance between responsiveness and stability, which is essential for effective voltage sag mitigation in grid-tied systems. Thus, although lower values of k_{sag} or overdamped configurations such as $k_{sag} = 6$ with $\alpha = 0.8$ provide stability, $k_{sag} = 6$ with $\alpha = 1$ offers the fastest response with acceptable oscillations, making it the most suitable choice for this application.

The performance of E^{+} under 50% voltage sag and 30% voltage swell is shown in Fig. 10 with different values of k_{sag}. The higher values of k_{sag} correspond to faster settling of E^{+} estimation.

D. Evaluation of eSOGI Performance With Bode Plot for Varying k and g Values

Fig. 11 shows the Bode plot of the eSOGI method for various k_{sag} and g_{sag} values. The magnitude plot indicates that increasing k_{sag} improves the system response at low frequencies,

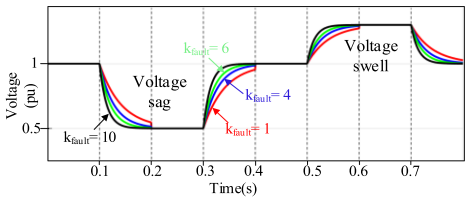

Fig. 10. Performance of E$^+$ Under 50 % Voltage Sag and 30 % Voltage swell.

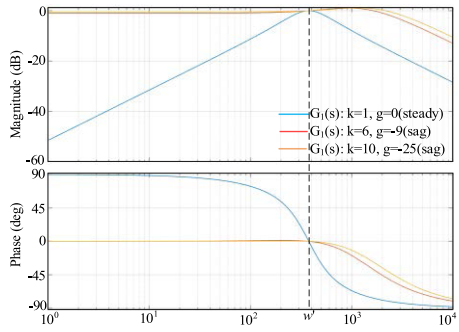

Fig. 11. Bode plot of eSOGI transfer function.

TABLE III
OPERATING SCHEME

Signals	Operation	Mode
λ_1=1, λ_2=0, λ_3=1, λ_4=0	Normal	GC
λ_1=0, λ_2=1, λ_3=1, λ_4=0	Transition	GC→IS
λ_1=0, λ_2=1, λ_3=0, λ_4=1	Normal	IS
λ_1=1, λ_2=0, λ_3=0, λ_4=1	Transition	IS→GC

allowing faster detection of disturbances such as voltage sags. However, this also increases sensitivity to higher frequencies, which can lead to instability. A higher k_{sag} value shifts the natural frequency, and a more negative g value creates a resonant peak, raising the risk of oscillations. Although higher k_{sag} values (e.g., $k_{sag} = 10$) results in faster disturbance detection, it may introduce oscillations, particularly during voltage recovery. Therefore, a balance is required between a fast response and system stability. Careful tuning of k_{sag} and g_{sag} ensures a quicker reaction to voltage sags while minimizing the potential for instability.

E. Smooth Switching Method for Seamless Transition Between GC and SA Modes

In this section, the objective is to propose a synchronization method to ensure optimal performance during the transitions between GC and SA modes. During grid faults, based on the trip times specified in IEEE 1547 and IEC 61727, transitions between the GC and SA modes should occur. Under these conditions, inaccurate grid voltage estimation can increase power fluctuations. This issue arises because grid voltages are used to derive the grid angle and synthesized grid current references. Consequently, significant transients can occur when switching from current control to voltage control. An accurate voltage estimation is achieved through the VBS. The synchronization for the two modes with the help of algorithm given in Table III

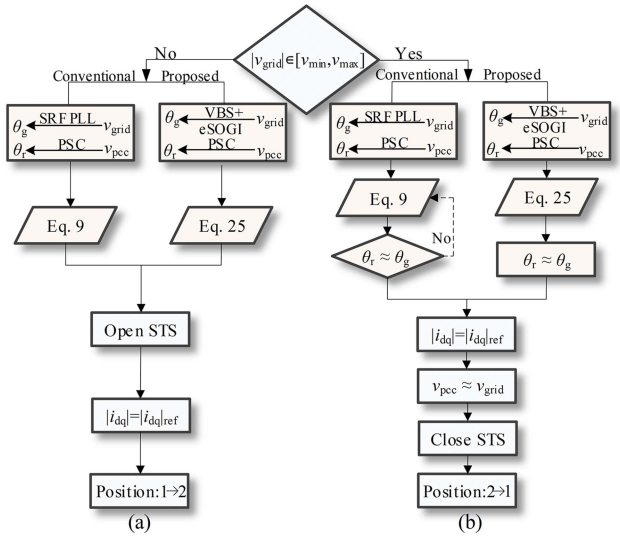

Fig. 12. Flowchart for transition between GC and SA modes. (a) GC to SA mode. (b) SA to GC mode.

is expressed as follows:

$$\theta(t) = \lambda_1\theta_g(t) + \lambda_2\theta_{\mathbf{r}}(t) + \lambda_3\theta_{\mathbf{g}}(t-1) + \lambda_4\theta_{\mathbf{r}}(t-1) \quad (25)$$

where λ_1, λ_2, λ_3, and λ_4 are constants.

The control methods of the GC and SA modes share the same inner current loop; thus, only the outer loop (a power loop for the GC mode and a voltage loop for the SA mode) requires regulation during mode transition. For a smooth transition between GC and SA modes, the reference values for the inner current loop should remain identical. During a GC mode transition, if the P_{ref} for both the control modes is identical, the output of the PSC matches that of the VBS under steady-state conditions. This alignment ensures smooth switching within the grid synchronization system. When switching from the SA to GC modes, the grid synchronization mechanism should shift from the PSC to the VBS. During this transition, the integrator output from the PSC should be changed using (25), and the switch in the grid synchronization system should be changed from position "2" to "1". In contrast, when switching from the GC to SA modes, the grid synchronization method should change from the VBS to the PSC. The integrator output from the VBS should be changed using (25), with the switch in the grid synchronization system moving from positions "1" to "2". The flowchart for the transition between GC and SA is shown in the Fig. 12.

1) Transition from GC to SA Modes.

a) When a voltage sag or swell occurs in the grid, a three-phase grid voltage results in the appearance of a negative-sequence component in the grid voltage. Positive-sequence voltages are used as the input voltages for the VBS, as depicted in Fig. 7, an accurate synchronization angle can still be obtained even during such voltage sags.

b) Upon detecting a fault on the grid, VBS is employed to accurately estimate the grid voltage. To protect the system, the STS is opened to disconnect the converter from the main grid.

c) Position "1" is then changed to "2", aligning the d-q reference voltages at the voltage controller to the same values. To avoid any abrupt change, the phase angles are changed as described in (25).
d) The converter subsequently switches its control strategy from power control mode to voltage control mode.

2) Transition from SA to GC Modes.
a) Determine whether the grid voltage is within the specified normal voltage range.
b) With the current loop at position "2", the positive-sequence voltages $e^{s+}_{\alpha\beta}$, derived from the measured three-phase grid voltage, are fed into the VBS algorithm. This adjusts the phase of the PCC voltage to synchronize it with the grid voltage, even under normal or unbalanced conditions.
c) With the current loop at position "2", the grid voltages in the *d-q* frame are used as reference commands for the voltage controller. This ensures that the PCC voltage magnitude is adjusted to match that of the grid voltage.
d) When both the phase and magnitude of the PCC voltage align with those of the grid voltage, the STS is closed, connecting the inverter to the main grid.
e) Once connected, the inverter switches from position "2" to "1" thereby shifting its control strategy from the voltage control to the power control mode.

IV. Simulation Results

The proposed and conventional methods were simulated on a 1-MW grid-tied system using the PLECS platform. The system operates at a maximum grid line voltage of 6.6 kV at 60 Hz. The dc link voltage was maintained at 10 kV, with a sampling interval of 0.1 ms. The switching frequency was set to 4 kHz. The eSOGI gains were selected as follows: $k_{\text{steady}} = 1$; $k_{\text{sag}} = 6$; $g_{\text{sag}} = -9$. Table IV shows the system parameters used in the simulation and experiment.

A. Transition From GC to SA Modes

The system performances during a transition from the GC to SA modes using the conventional and proposed methods are illustrated in Figs. 13 and 14, respectively, under 50% balanced sags and in Figs. 15 and 16, respectively, under unbalanced voltage sags; (a) shows the STS status, (b) shows the grid voltages, (c) shows the active and reactive power of the load, (d) shows the *dq*-axis load current component, (e) shows the positive-sequence *dq*-axis PCC voltage, and (f) shows the grid currents. Here, the conventional method represents the SRF-PLL with a PI-based presynchronization scheme. Peak load current and peak active power during the voltage sag and the transition time for the four different scenarios are listed in Table V.

Fig. 13(c) shows the peak active power of 1.125 MW during the sag and 1.091 MW during the transition. Fig. 14(c) depicts 1 and 1.095 MW, respectively, for the same periods. Similarly, Fig. 13(d) shows peak load currents of 220 A during the sag and 202 A during the transition, compared to 175 and 187 A, respectively, shown in Fig. 14(d). For a precise comparison, it should be noted that the expected load current at the onset of the sag and during the transition should be approximately 174.95 A.

TABLE IV
Parameters of Simulation and Experiment

Details	Unit	Value (Simulation)	Value (Experiment)
Rated Power	kW	1000	1
Line voltage	V	6600	141
Dc link voltage	V	10000	200
SM voltage	V	2500	50
SM capacitance	mF	2.2	2
Arm inductor	mH	2.5	2.5
Filter capacitor	μF	2.11	2.11
Filter inductor	mH	3	3
Load resistance	Ω	21.78	10
Switching freq.	kHz	4	4
Controller Parameters			
Bandwidth of SRF-PLL		15 rad/s	10 rad/s
Bandwidth of power loop		120 rad/s	50 rad/s
Bandwidth of voltage loop		25 rad/s	12 rad/s
Bandwidth of current loop		1100 rad/s	600 rad/s
Bandwidth of PI-based method		62 rad/s	60 rad/s
Cut-off frequency of LPF		100 rad/s	100 rad/s
eSOGI parameters(k_{sag})		6	6
eSOGI parameters (g_{sag})		-9	-9
eSOGI parameters(k_{steady})		1	1

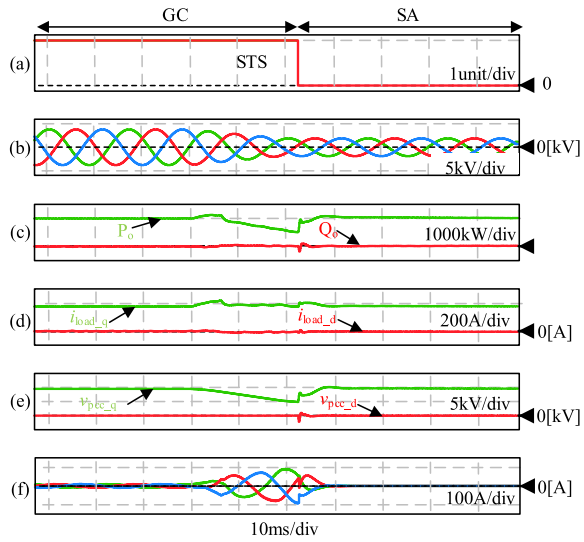

Fig. 13. Control performance during GC to SA mode transition using conventional method under balanced sag. (a) STS status. (b) Three-phase grid voltages. (c) Active and reactive power of load. (d) Positive-sequence *dq*-axis load current component. (e) Positive-sequence *dq*-axis PCC voltage component. (f) Grid currents.

The peak voltage during the transition is 4086 V, as shown in Fig. 13(e), whereas Fig. 14(e) shows 4000 V. Fig. 13(f) shows a peak grid current of 92 A, which decreases to 86 A in Fig. 14(f).

The proposed method reduces the settling time after the transition to 0.8 ms compared to 9.4 ms for the conventional method. The power fluctuation is also lowered, decreasing from 125 to 93 kW. In addition, it reduces the load current fluctuation from 24.60% to 6.89%.

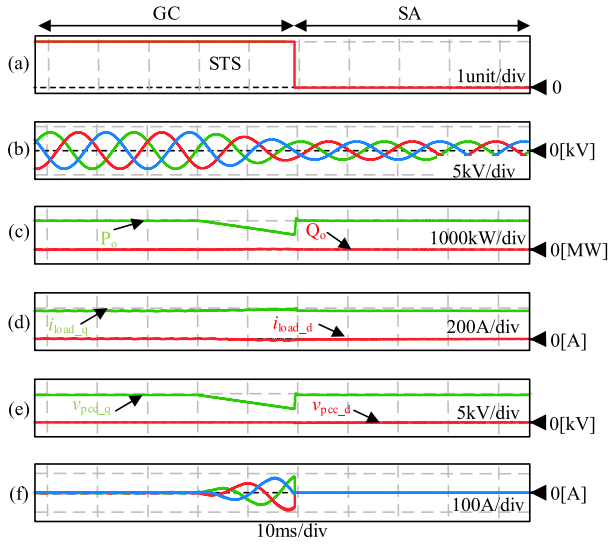

Fig. 14. Control performance during GC to SA mode transition using proposed method under balanced sag. (a) STS status. (b) Grid voltages. (c) Active and reactive power of load. (d) Positive-sequence *dq*-axis load current component. (e) Positive-sequence *dq*-axis PCC voltage component. (f) Grid currents.

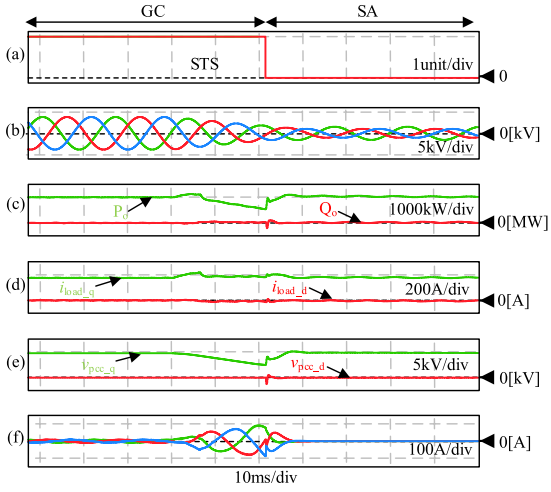

Fig. 15. Control performance during GC to SA mode transition using conventional method under unbalanced sag. (a) STS status. (b) Three-phase grid voltages. (c) Active and reactive power of load. (d) Positive-sequence *dq*-axis load current component. (e) Positive-sequence *dq*-axis PCC voltage component. (f) Grid currents.

TABLE V
ANALYSIS OF SIMULATION RESULTS

Mode transition from GC to SA					
Cases	Parameters	Conventional method		Proposed method	
		During sag	During transition	During sag	During transition
Balance voltage sag	i_{load_q} (A)	218	202.7	176	187
	P_o (MW)	1.12	1.08	1	1.09
	t_s (ms)	20.6	9.4	19.2	0.8
Unbalance voltage sag	i_{load_q} (A)	220	202	175	187
	P_o (MW)	1.12	1.09	1	1.09
	t_s (ms)	22.6	8.4	19.3	0.7

Mode transition from SA to GC		
Parameter	Conventional method	Proposed method
t_s (ms)	106	61.2

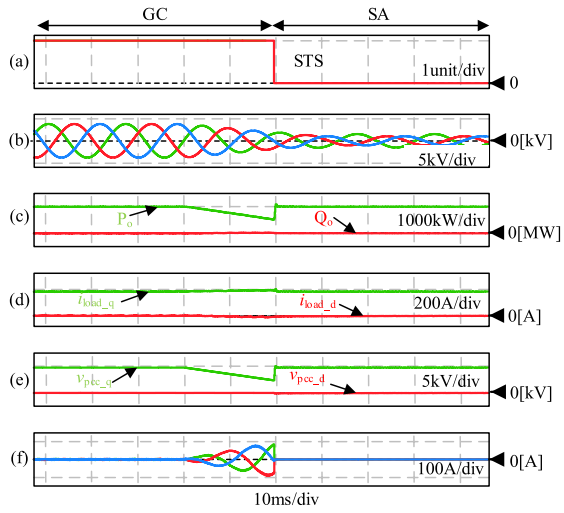

Fig. 16. Control performance during GC to SA mode transition using proposed method under unbalanced sag. (a) STS status. (b) Three-phase grid voltages. (c) Active and reactive power of load. (d) Positive-sequence *dq*-axis load current component. (e) Positive-sequence *dq*-axis PCC voltage component. (f) Grid currents.

Fig. 15(c) shows the peak active power of 1.125 MW during the sag and 1.083 MW during the transition; Fig. 16(c) shows 1 and 1.093 MW, respectively, for the same periods. The peak load current decreases from 218 and 203 A during the sag and transition, respectively, in Fig. 15(d) to 176 and 187 A, respectively, in Fig. 16(d). The peak voltage during the transition is 4070 V, as indicated in Fig. 15(e), compared to 4020 V in Fig. 16(e). Fig. 15(f) highlights a peak grid current of 90 A, which decreases to 86 A in Fig. 16(f).

The proposed method shortens the settling time to 0.7 ms, a decrease from 8.6 ms. The power fluctuation decreases to 95 kW compared to 125 kW with the conventional method. In addition, the load current fluctuation decreased from 25.75% to 6.89%.

These results emphasize the advantages of the proposed method, highlighting faster transitions, reduced power and current fluctuations, and enhanced system stability during voltage sags.

B. Transition From SA to GC Modes

The system performances during the transition from the SA to GC modes using the conventional and proposed synchronization methods are shown in Figs. 17 and 18, respectively; (a) shows the grid voltages, (b) shows the PCC voltages, (c) shows the load currents, (d) shows the A-phase grid and PCC voltages, (e) shows STS status, and (f) shows the phase angles.

Once the frequency of the PCC voltage and the grid voltage remain within the specified limit, as shown in Table I, the transition process can begin. The PCC voltage is first synchronized with the grid voltage, as shown in Fig. 17(d). Once the phase error between the grid and PCC voltages is reduced to within the 2° tolerance, the magnitude of the PCC voltage is adjusted to match the grid voltage. After both the phase and magnitude of the PCC voltage are synchronized with those of the grid voltage, the STS is closed, and the inverter operation changes from the SA

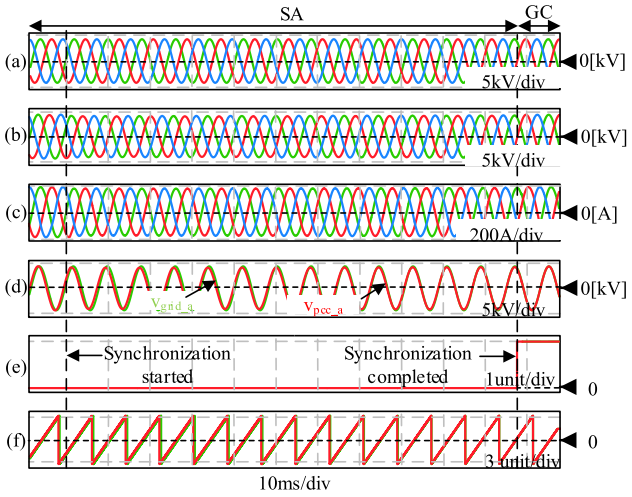

Fig. 17. Control performance during SA to GC mode transition using the conventional method. (a) Grid voltages. (b) PCC voltages. (c) Load currents. (d) A-phase grid and PCC voltages. (e) STS status. (f) Phase angles.

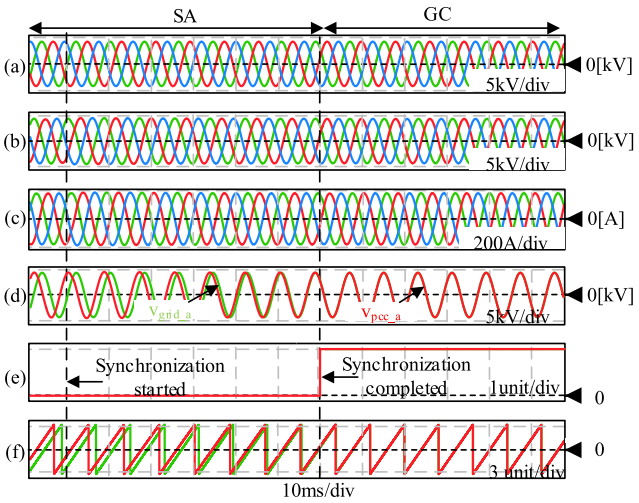

Fig. 18. Control performance during SA to GC mode transition using the proposed method. (a) Grid voltages. (b) PCC voltages. (c) Load currents. (d) A-phase grid and PCC voltages. (e) STS status. (f) Phase angles.

mode to GC mode. The duration of the synchronization process and the transfer of control to the GC mode is 106 ms, whereas Fig. 18(d) shows a duration of 61.2 ms for the change of control to the GC mode. Fig. 17(e) illustrates the synchronization of the grid and PCC phases, compared to the synchronization process shown in Fig. 18(e).

The proposed synchronization method demonstrates a faster response time, outperforming the conventional method by 44.8 ms. Table V presents the simulation results. The results confirm that the converter can smoothly transition from SA to GC operations using the proposed method.

V. Experimental Results

Experiments were conducted to validate the effectiveness of the proposed method for a 1-kW prototype. The parameters of the hardware setup, illustrated in Fig. 19, are detailed in Table III. The controller was implemented using the TMS320F28335 DSP

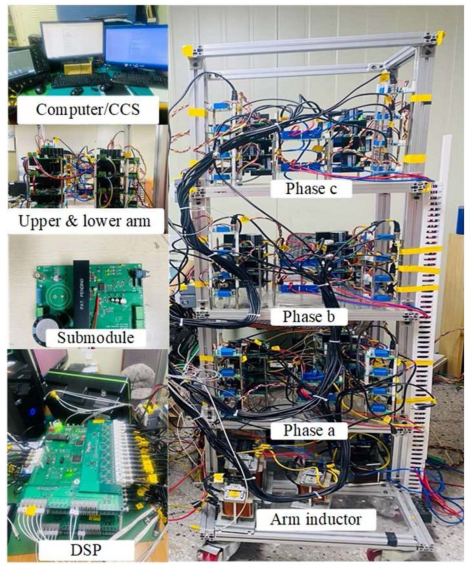

Fig. 19. Experimental set-up.

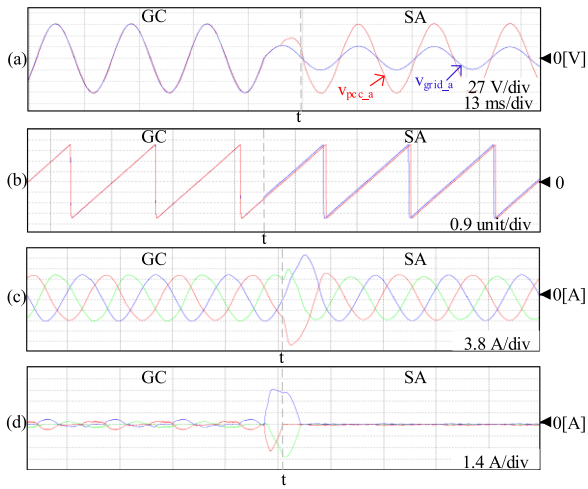

Fig. 20. Control performance during the GC to SA mode transition using conventional method. (a) A-phase grid and PCC voltages. (b) Phase angles. (c) Load currents. (d) Grid currents.

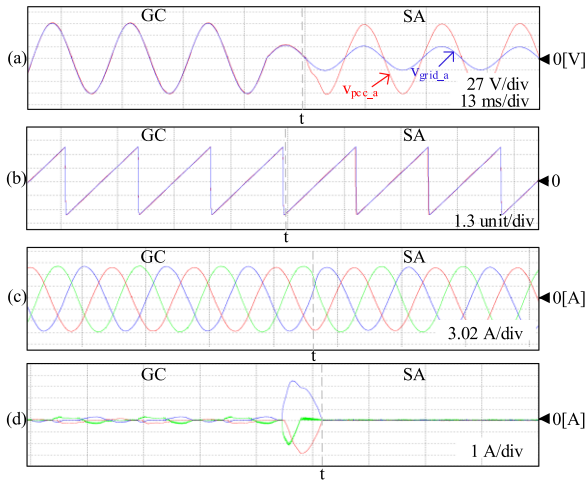

Fig. 21. Control performance during the GC to SA mode transition using proposed method. (a) A-phase grid and PCC voltages. (b) Phase angles. (c) Load currents. (d) Grid currents.

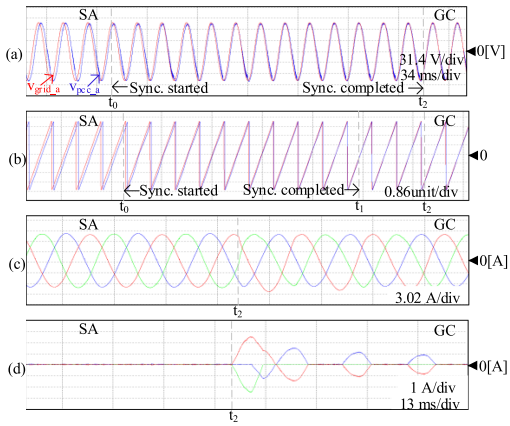

Fig. 22. Control performance during the SA to GC mode transition using conventional method. (a) A-phase grid and PCC voltages. (b) Phase angles. (c) Load currents. (d) Grid currents.

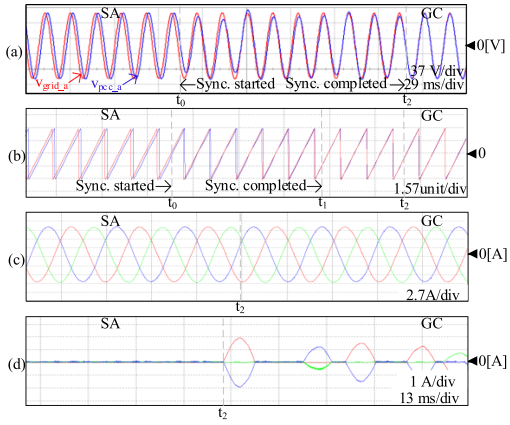

Fig. 23. Control performance during the SA to GC mode transition using proposed method. (a) A-phase grid and PCC voltages. (b) Phase angles. (c) Load currents. (d) Grid currents.

and XC3S400-PQ208 FPGA from Texas Instruments. FPGA processes the input–output functions, such as analog-to-digital converter from the sensor data and generates pulsewidth modulation signals for the gate drivers. A dc power supply is connected to the dc-link capacitor to maintain a stable dc-link voltage. An ac power supply is connected to the converter output via an *LC* filter to ensure an ac grid voltage. The dc-link voltage is maintained at 200 V. A five-level MMC was employed as the converter, featuring four submodules per arm. The switching frequency was 4 kHz.

The system performances with the conventional and proposed methods were investigated. The results obtained during GC to SA mode transitions, are presented in Figs. 20 and 21, respectively. The results obtained during SA to GC mode transitions are presented in Figs. 22 and 23, respectively; (a) shows the A-phase grid and PCC voltages, (b) shows the phase angles, (c) shows the three-phase load currents, and (d) shows the three-phase grid currents.

When the grid voltage sags below 50%, the system transitions from the GC to SA modes. Figs. 20(b) and 21(b) show the phase angles of the grid and PCC voltages. Fig. 20(c) shows a peak load current of 17.48 A during the transition, whereas Fig. 21(c)

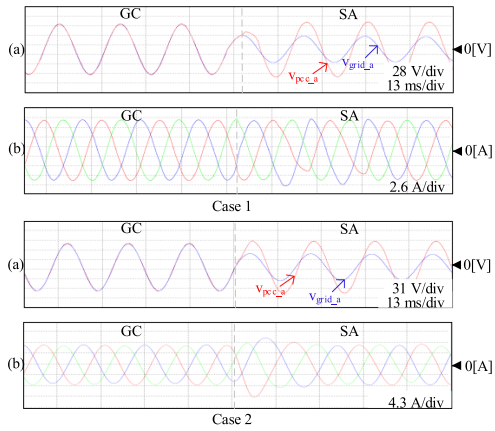

Fig. 24. Control performance during the GC to SA mode transition using different k_{sag} and g_{sag} values. (a) A-phase grid and PCC voltages. (b) Load currents. Case 1: k_{sag}= 1, g_{sag}= 0. Case 2: k_{sag} = 10, g_{sag} = −25.

shows a peak current of 8.2 A. Similar to the simulation results, these load current fluctuations are lower than those observed when using the conventional method. Appropriate tuning of the presynchronization method can help reduce these transients in the conventional approach. Fig. 20(d) shows that the grid current initially increases during the voltage sag. It then decreases to zero, with a peak value of 4.2 A. In contrast, Fig. 21(d) shows a grid current peak of 3.4 A. The proposed method demonstrates a seamless transition in the load current, indicating smoother performance.

Fig. 22(a) shows the A-phase of the grid and PCC voltages. "t_0" represents the instant when phase synchronization begins, "t_1" marks the moment when the grid voltage and PCC voltage synchronize, and "t_2" indicates the transition point when the STS closes. Upon receiving the mode transition signal, the phase of the PCC voltage is first synchronized with the grid voltage. After synchronization, their magnitudes are equalized. The transition from the SA to GC modes is completed once both the phase and magnitude of the PCC and grid voltages matches. The duration of the transition was observed to be 210.8 ms. Similarly, as shown in Fig. 23(a), upon receiving the mode transition signal, the magnitudes of the PCC and grid voltages are equalized. Once the voltage magnitudes match, the control shifts from the SA to GC mode. The transition time is 150.8 ms. Fig. 22(b) shows the phase angle of the PCC and grid voltages. The time taken for both phases to synchronize is 158.2 ms, whereas the proposed method achieves synchronization in 99.9 ms, as shown in Fig. 23(b). Fig. 22(c) shows a load current peak of 9.2 A, whereas Fig. 23(c) shows a peak of 8.175 A. Fig. 22(d) shows a grid current peak of 2.5 A, whereas Fig. 23(d) shows a peak of 1.9 A. The proposed synchronization method exhibits a faster response time, outperforming the conventional method by 60 ms.

The system performance for different k_{sag} and g_{sag} values during the GC to SA mode transition is shown in Fig. 24; Fig. 24(a) shows the A-phase grid and PCC voltages, whereas Fig. 24(b) shows the three-phase load currents. In Case 1 (k_{sag} = 1, g_{sag} = 0), the transition is slower, with a peak load current of 10.16 A. The waveform is not fully sinusoidal due to the extended settling time. In Case 2 (k_{sag} = 10, g_{sag} = −25),

the response is faster, but the peak load current increases to 12.4 A with noticeable oscillations. The root locus and Bode plot confirm that higher k_{sag} improves disturbance detection but increases high-frequency sensitivity, leading to transient oscillations.

VI. Conclusion

In this article, an advanced seamless transition approach for critical infrastructures between the GC and SA modes has been proposed. The proposed method addresses the limitations of SRF-PLL by providing faster and more accurate voltage estimation during voltage sags. The use of an angle alignment method instead of a PI-based method for presynchronization enhances the transition between the GC and SA modes, reducing phase mismatches and allowing faster transitions. Simulations on a 1-MW system showed a 44.8 ms improvement in the transition response time from the SA to GC modes. During the GC to SA mode transition, the load current fluctuation was reduced from 25.75% to 6.89%. Experimental validation on a 1-kW system confirmed stable and smooth transitions with minimal disturbances of the load current. The combined use of the VBS technique with the dual-eSOGI method for voltage estimation and the angle alignment method for presynchronization results in a reliable and effective solution for grid-tied systems. The proposed approach is well suited for ensuring seamless power delivery under grid disturbances, improving system reliability and response time.

References

[1] F. BlaaBjerg, Y. Yang, D. Yang, and X. Wang, "Distributed power-generation systems and protection," *Proc. IEEE*, vol. 105, no. 7, pp. 1311–1331, Jul. 2017, doi: 10.1109/JPROC.2017.2696878.

[2] A. Micallef, M. Apap, C. S.- Staines, and J. M. Guerrero, "Single-phase microgrid with seamless transition capabilities between modes of operation," *IEEE Trans. Smart Grid*, vol. 6, no. 6, pp. 2736–2745, Nov. 2015, doi: 10.1109/TSG.2015.2444912.

[3] "IEEE standard for interconnection and interoperability of distributed energy resources with associated electric power systems interfaces amendment-amendment 1: To provide more flexibility for adoption of abnormal operating performance category iii," *IEEE Std 1547a-2020 (Amendment to IEEE Std 1547-2018)*, pp. 1–16, 15, Apr. 2020, doi: 10.1109/IEEESTD.2020.9069495.

[4] T. Hwang and S. Park, "A seamless control strategy of distributed generation inverter for critical load safety under strict grid disturbance," in *Proc. 27th Annu. IEEE Appl. Power Electron. Conf. Expo.*, 2012, pp. 254–261, doi: 10.1109/APEC.2012.6165828.

[5] G.-C. Hsieh and J. C. Hung, "Phase-locked loop techniques-a survey," *IEEE Trans. Ind. Electron.*, vol. 43, no. 6, pp. 609–615, Dec. 1996, doi: 10.1109/41.544547.

[6] J. C. Vasquez, J. M. Guerrero, A. Luna, P. Rodríguez, and R. Teodorescu, "Adaptive droop control applied to voltage-source inverters operating in grid-connected and islanded modes," *IEEE Trans. Ind. Electron.*, vol. 56, no. 10, pp. 4088–4096, Oct. 2009, doi: 10.1109/TIE.2009.2027921.

[7] L. Rolim, D. da Costa, and M. Aredes, "Analysis and software implementation of a robust synchronizing PLL circuit based on the PQ theory," *IEEE Trans. Ind. Electron.*, vol. 53, no. 6, pp. 1919–1926, Dec. 2006, doi: 10.1109/TIE.2006.885483.

[8] K.-G. Masoud, "Universal integrated synchronization and control for single-phase DC/AC converters," *IEEE Trans. Power Electron.*, vol. 30, no. 3, pp. 1544–1557, Mar. 2015, doi: 10.1109/TPEL.2014.2304459.

[9] S. Wenjia and F. Jingyang, "Transient stability improvement of grid-forming converters through voltage amplitude regulation and reactive power injection," *IEEE Trans. Power Electron.*, vol. 38, no. 1, pp. 12116–12125, Oct. 2023, doi: 10.1109/TPEL.2023.3290170.

[10] M. Karimi-Ghartemani and M. R. Iravani, "A method for synchronization of power electronic converters in polluted and variable-frequency environments," *IEEE Trans. Power Syst.*, vol. 19, no. 3, pp. 1263–1270, Aug. 2004, doi: 10.1109/TPWRS.2004.831280.

[11] J. Chen, M. Liu, and H. Geng, "Impact of PLL frequency limiter on synchronization stability of grid feeding converter," *IEEE Trans. Power Syst.*, vol. 37, no. 3, pp. 2487–2490, May 2022, doi: 10.1109/TPWRS.2022.3145636.

[12] X. Meng, X. Liu, M. He, Z. Liu, and J. Liu, "A self-adaptive controller for inverter with seamless transfer and automatic pre-synchronization capability," *IEEE Access*, vol. 8, no. 1, pp. 105936–105949, 2020, doi: 10.1109/ACCESS.2020.3000268.

[13] N. Beniwal, I. Hussain, and B. Singh, "Vector-based synchronization method for grid integration of solar PV-battery system," *IEEE Trans. Ind. Inform.*, vol. 15, no. 9, pp. 4923–4933, Sep. 2019, doi: 10.1109/TII.2019.2921034.

[14] B. Singh, G. Pathak, and B. K. Panigrahi, "Seamless transfer of renewable-based microgrid between utility grid and diesel generator," *IEEE Trans. Power Electron.*, vol. 33, no. 10, pp. 8427–8437, Oct. 2018, doi: 10.1109/TPEL.2017.2778104.

[15] S. Kewat and B. Singh, "Robust control for islanded and seamless mode switching of wind – PV grid-tied generation system," *IEEE Trans. Ind. Appl.*, vol. 57, no. 5, pp. 5285–5295, Sep./Oct. 2021, doi: 10.1109/TIA.2021.3087544.

[16] Z. Liu and J. Liu, "Indirect current control based seamless transfer of three-phase inverter in distributed generation," *IEEE Trans. Power Electron.*, vol. 29, no. 7, pp. 3368–3383, Jul. 2014, doi: 10.1109/TPEL.2013.2282319.

[17] F. Tang, J. M. Guerrero, J. C. Vasquez, D. Wu, and L. Meng, "Distributed active synchronization strategy for microgrid seamless reconnection to the grid under unbalance and harmonic distortion," *IEEE Trans. Smart Grid*, vol. 6, no. 6, pp. 2757–2769, Nov. 2015, doi: 10.1109/TSG.2015.2406668.

[18] Q.-C. Zhong, P.-L. Nguyen, Z. Ma, and W. Sheng, "Self-synchronized synchronverters : Inverters without a dedicated synchronization unit," *IEEE Trans. Power Electron.*, vol. 29, no. 2, pp. 617–630, Feb. 2015, doi: 10.1109/TPEL.2013.2258684.

[19] M. Ramezani, S. Li, F. Musavi, and S. Golestan, "Seamless transition of synchronous inverters using synchronizing virtual torque and flux linkage," *IEEE Trans. Ind. Electron.*, vol. 67, no. 1, pp. 319–328, Jan. 2020, doi: 10.1109/TIE.2019.2892697.

[20] X. Meng, H. Guo, X. Wang, M. He, and J. Liu, "Seamless transition for parallel inverters with novel self-adaptive hybrid controller and presynchronization unit," *IEEE J. Emerg. Sel. Topics Power Electron.*, vol. 10, no. 5, pp. 5819–5832, Oct. 2022, doi: 10.1109/JESTPE.2022.3161586.

[21] T.-V. Tran, T.-W. Chun, H.-H. Lee, H.-G. Kim, and E.-C. Nho, "PLL-based seamless transfer control between grid-connected and islanding modes in grid-connected inverters," *IEEE Trans. Power Electron.*, vol. 29, no. 10, pp. 5218–5228, Oct. 2014, doi: 10.1109/TPEL.2013.2290059.

[22] D. Dong, B. Wen, D. Boroyevich, P. Mattavelli, and Y. S. Xue, "Analysis of phase-locked loop low-frequency converters considering impedance interactions," *IEEE Trans. Ind. Electron.*, vol. 62, no. 1, pp. 310–321, Jan. 2015, doi: 10.1109/TIE.2014.2334665.

[23] J. Wang, A. Pratt, and M. Baggu, "Integrated synchronization control of grid-forming inverters for smooth microgrid transition," in *Proc. IEEE Power Energy Soc. Gen. Meeting*, 2019, pp. 1–5. doi: 10.1109/PESGM40551.2019.8973453.

[24] M. N. Arafat, S. Palle, Y. Sozer, and I. Husain, "Transition control strategy between standalone and grid-connected operations," *IEEE Trans. Ind. Appl.*, vol. 48, no. 5, pp. 1516–1525, Sep./Oct. 2012, doi: 10.1109/TIA.2012.2210013.

[25] T. L. Vandoorn, B. Meersman, J. D. M. D. Kooning, and L. Vandevelde, "Transition from islanded to grid-connected mode of microgrids with voltage-based droop control," *IEEE Trans. Power Syst.*, vol. 28, no. 3, pp. 2545–2553, Aug. 2013, doi: 10.1109/TPWRS.2012.2226481.

[26] A. Nigam and D.-C. Lee, "Seamless transition strategies of MMC-based grid forming /following inverter systems for critical loads," in *Proc. IEEE Energy Convers. Congr. Expo.*, 2024, pp. 1–7.

[27] R. Teodorescu, M. Liserre, and P. Rodriguez, *Grid Converters for Photovoltaic and Wind Power Systems*. New York, NY, USA: Wiley, 2011.

[28] A. T. Nguyen and D.-C. Lee, "Advanced grid synchronization scheme based on dual eSOGI-FLL for grid-feeding converters," *IEEE Trans. Power Electron.*, vol. 37, no. 6, pp. 7218–7229, Jun. 2022, doi: 10.1109/TPEL.2022.3140893.

[29] F. Sevilmi and H. Karaca, "Performance enhancement of DSOGI-PLL with a simple approach in grid-connected applications," *Energy Rep.*, vol. 8, pp. 9–18, 2022, doi: 10.1016/j.egyr.2021.11.186.

Anupam Nigam (Graduate Student Member, IEEE) was born in Lucknow, India, in 1996. He received the B.E. degree in electrical engineering from LNCT, Bhopal, India, in 2018, and the M.Tech. degree in energy engineering from the Indian Institute of Technology, Mandi, India, in 2021. He is currently working toward the Ph.D. degree in electrical engineering with Yeungnam University, Gyeongsan, South Korea.

His research interests include seamless transition between grid-forming and grid-following inverters, current-constrained control of grid-forming converters, and modular multilevel converters for renewable energy integration.

Dong-Choon Lee (Fellow, IEEE) received the B.S., M.S., and Ph.D. degrees in electrical engineering from Seoul National University, Seoul, South Korea, in 1985, 1987, and 1993, respectively.

He was a Research Engineer with Daewoo Heavy Industry, South Korea, from 1987 to 1988. He has been a faculty member with the Department of Electrical Engineering, Yeungnam University, Gyeongsan, South Korea, since 1994. He was a Visiting Scholar with the Power Quality Laboratory, Texas A&M University, College Station, TX, USA, in 1998; the Electrical Drive Center, University of Nottingham, Nottingham, ENG, U.K., in 2001; the Wisconsin Electric Machines and Power Electronics Consortium, University of Wisconsin, Madison, WI, USA, in 2004; the FREEDM Systems Center, North Carolina State University, Raleigh, NC, USA, from Sep. 2011 to Aug. 2012. His current research interests include power converter design and control, renewable energy and its grid connection, ac machine drives, and dc power system.

Dr. Lee was the Editor-in-Chief of the *Journal of Power Electronics* of the Korean Institute of Power Electronics (KIPE), from 2015 to 2017. In 2019, he was the President with KIPE. He also was the General Chair of ICPE 2023-ECCE Asia held in Jeju, South Korea. He is currently an Associate Editor for IEEE TRANSACTIONS ON POWER ELECTRONICS and the Chair of the IEEE Taegu Section PELS Chapter.